High-resolution cell outline segmentation and tracking from phase-contrast microscopy images

Ambühl, Mark E ; Brepsant, Charles ; Meister, Jean-Jacques ; Verkhovsky, Alexander B ; Sbalzarini, Ivo F

Abstract: Accurate extraction of cell outlines from microscopy images is essential for analysing the dynamics of migrating cells. Phase-contrast microscopy is one of the most common and convenient imaging modalities for observing cell motility because it does not require exogenous labelling and uses only moderate light levels with generally negligible phototoxicity effects. Automatic extraction and tracking of high-resolution cell outlines from phase-contrast images, however, is difficult due to complex and non-uniform edge intensity. We present a novel image-processing method based on refined level-set segmentation for accurate extraction of cell outlines from high-resolution phase-contrast images. The algorithm is validated on synthetic images of defined noise levels and applied to real image sequences of polarizing and persistently migrating keratocyte cells. We demonstrate that the algorithm is able to reliably reveal fine features in the cell edge dynamics.

DOI: https://doi.org/10.1111/j.1365-2818.2011.03558.x

High-resolution cell outline segmentation and tracking from phase-contrast microscopy images

Journal:	*Journal of Microscopy*
Manuscript ID:	JMI-2011-0029.R3
Wiley - Manuscript type:	Original Article
Date Submitted by the Author:	n/a
Complete List of Authors:	Ambühl, Mark; EPFL, IPSB Brepsant, Charles; EPFL, IPSB Meister, Jean-Jacques; EPFL, IPSB Verkhovsky, Alexander; EPFL; EPFL, IPSB Sbalzarini, Ivo; ETH Zurich, Computer Science
Keywords:	cell motility, cell polarization, phase-contrast microscopy, edge detection, near-optimal thresholding, level-set segmentation, cell shape, cell outline tracking

High-resolution cell outline segmentation and tracking from phase-contrast microscopy images

M. E. Ambühl* C. Brepsant* J-J. Meister*

A. Verkhovsky* I. F. Sbalzarini†

August 12, 2011

Keywords: Cell motility, cell polarization, phase-contrast microscopy, edge detection, near-optimal thresholding, level-set segmentation, cell shape, cell outline tracking

Correspondence to: Prof. Ivo F. Sbalzarini, Email: ivos@ethz.ch

*Laboratory of Cell Biophysics, EPF Lausanne, SG-AAB Station 15, Lausanne, Switzerland

†Institute of Theoretical Computer Science and Swiss Institute of Bioinformatics, ETH Zurich, Universitätstrasse 6, CAB E64, CH-8092 Zürich, Switzerland

Abstract

Accurate extraction of cell outlines from microscopy images is essential for analyzing the dynamics of migrating cells. Phase-contrast microscopy is one of the most common and convenient imaging modalities for observing cell motility since it does not require exogenous labeling and uses only moderate light levels with generally negligible phototoxicity effects. Automatic extraction and tracking of high-resolution cell outlines from phase-contrast images, however, is difficult due to complex and non-uniform edge intensity. We present a novel image-processing method based on refined level-set segmentation for accurate extraction of cell outlines from high-resolution phase-contrast images. The algorithm is validated on synthetic images of defined noise levels and applied to real image sequences of polarizing and persistently migrating keratocyte cells. We demonstrate that the algorithm is able to reliably reveal fine features in the cell edge dynamics.

1 Introduction

Cell migration is based on the interplay of forces arising from different sources such as actin-polymerization pressure at the cell edge (Mogilner & Oster, 1996; Pantaloni *et al.*, 2001; Mogilner & Oster, 2003), myosin-dependent contraction of the actin network (Svitkina *et al.*, 1997; Verkhovsky *et al.*,

1999), adhesion to the extracellular matrix (Mitchison, 1996; Anderson & Cross, 2000; Fournier *et al.*, 2010), and membrane tension (Keren *et al.*, 2008). Changes in cell shape constitute macroscopic manifestations of these intracellular molecular processes. Studies of cell motility and the involved machinery hence depend on observing the dynamically changing shapes of migrating cells (Pincus & Theriot, 2007). On the one hand, analysis of cell shape can provide insights into the internal mechanics of actin polymerization and membrane tension (Keren *et al.*, 2009). On the other hand, cell shape dynamics can be simulated based on specific hypotheses about the internal dynamics (Satulovsky *et al.*, 2008) and compared to experimentally observed shapes. All of these studies rely on accurate information about the cell edge position and its evolution, requiring computational image segmentation and shape tracking methods.

Manual segmentation is often prohibitive due to the large number of images that need to be analyzed and the high level of accuracy and reproducibility required; small errors in subjective manual segmentation can result in large relative errors when analyzing small cell-edge displacements over short time intervals. While automatic contour extraction is increasingly common in fluorescence microscopy (Machacek & Danuser, 2006; Russell *et al.*, 2009; Helmuth *et al.*, 2009; Helmuth & Sbalzarini, 2009), accurate and robust procedures for phase-contrast images are less well developed (Hand *et al.*, 2009).

Phase-contrast microscopy, however, is the preferred source of information when studying cell motility. It provides good contrast for cell edge detection without exogenous dyes, uses only moderate levels of light, and is free from artifacts of bleaching and photo-damage as are common in fluorescence microscopy. If phase-contrast microscopy is used in conjunction with fluorescence microscopy, using the phase-contrast channel for edge detection frees additional fluorescence channels for observing intracellular markers.

Automatic cell segmentation from phase-contrast images, however, is challenging and standard segmentation approaches used for fluorescently labeled cells are ineffective. The bright halo surrounding a cell in a phase-contrast image misleads edge detectors to produce spurious edges. Threshold-based approaches cannot be used due to the shadeoff effect inherent to phase-contrast devices, which equalizes the background and cell gray levels (Otaki, 2000). Several attempts have been made to overcome these problems. Grimm *et al.* (2003) used an active contour ("snake") algorithm (Kass *et al.*, 1988) to detect the position of the cell's leading edge in phase-contrast images. Li *et al.* (2009) augmented this approach by guiding the active contour with the vector flow of the leading protrusion. Their procedure, however, does not work reliably for the trailing edge, and would be difficult to extend to the irregular motion of polarizing cells. Weak watershed transform assembly has been used by Debeir *et al.* (2008), but in this approach the cell's cen-

troid needed to be marked prior to segmentation. In a different approach, a statistical procedure using pattern recognition techniques (Bradhurst *et al.*, 2009) has been used, relying on prior knowledge about the cell shape. Completely automatic algorithms for detecting and tracking large numbers of cells in phase-contrast images have also been presented (Hand *et al.*, 2009; Li *et al.*, 2008). These approaches emphasize tracking performance using concepts from, e.g., image registration (Hand *et al.*, 2009) or multi-model motion filtering (Li *et al.*, 2008). Typically, however, these approaches are designed for low-resolution images and do not provide high-resolution cell outline geometries.

Here, we describe a novel automated procedure for segmenting and tracking cell outlines of arbitrary shape from high-resolution phase-contrast images containing small numbers of cells. Our approach is based on a combination of near-optimal thresholding, morphological operations, and level-set segmentation with an adapted energy functional. We validate our method using simulated images and apply it to quantify cell edge dynamics in a model system of polarizing and migrating fish epidermal keratocytes.

Fish keratocytes are a well-established system for cell motility studies (Goodrich, 1924; Keren *et al.*, 2008; Lee *et al.*, 1993). In a polarized migratory state they are characterized by a regular and stable shape as described by the Graded Radial Extension (GRE) model (Lee *et al.*, 1993). The GRE

model is based on the assumption that keratocytes maintain the overall curvature of their leading edge during migration, but the detailed distribution of protrusion rates at the leading edge has not been characterized. We analyze keratocyte edge dynamics in regular migrating cells as well as in the more complex case of cells undergoing initial polarization (Yam *et al.*, 2007). In the latter case, the present algorithm is able to identify dynamic protrusion/retraction oscillations of the edge.

2 Cell outline segmentation and tracking algorithm

The present segmentation algorithm relies on a two-step procedure to extract accurate and smooth representations of cell outlines from phase-contrast microscopy images. The first step aims at roughly separating the image area containing the cell of interest (i.e., the foreground) from the background, as well as from areas containing other cells possibly present in the same image. This is done by near-optimal thresholding. The second step then determines the accurate outline shape of the cell of interest to sub-pixel resolution by evolving a geometric active contour (Kass *et al.*, 1988; Malladi *et al.*, 1995; Caselles *et al.*, 1993; Osher & Sethian, 1988) according to an adapted level-

set equation with an energy term suitably chosen for phase-contrast images. The algorithm as presented here segments and tracks a single cell per image/movie. If several cells are present in the field of view, the user may choose which cell to track, else the algorithm selects the largest cell by default. This is a design choice of the algorithm, rather than an inherent limitation of the methods used. Level-set methods also allow segmenting and tracking several objects per image. This was, however, not needed in the present application.

2.1 Initial foreground/background separation

Phase-contrast microscopy translates minute variations in light phase into perceivable changes in amplitude, hence improving image contrast when observing objects with a different optical path length (e.g., due to a different refractive index) than the surrounding medium. Phase-contrast microscopes, however, produce a number of artifacts that complicate image analysis. These include halos and shadeoffs (Otaki, 2000) that mostly prohibit the application of standard edge-detection algorithms. In our setting, bright halos appear around the cells with an intensity and width that depend on the local thickness of the cell. Shadeoff equalizes the intensity of the inner and outer regions of a large object to the same value, additionally complicating the separation between foreground and background and hampering

Figure 1: Figure 1 here

the use of thresholding techniques. The latter artifact is significant in our application since reconstructing precise cell outlines requires high imaging resolution, such that the observed cell covers a large portion of the field of view. These imaging artifacts are clearly visible in Figs. 2(b), 3(c), and 3(d).

In the first step of the present image-processing procedure, we exploit the fact that the halo has a different intensity than both the fore- and background in order to construct a rough estimate of the cell edge by taking a suitably chosen threshold on the gradient of the original image. The desired value of the threshold is not known *a priori* and may depend on several experimental parameters. This may include controllable parameters such as exposure time and magnification[1], but also uncontrollable parameters such as camera noise, the shape of the cell, and the number of cells in an image. We here suggest a generic method to automatically find a near-optimal threshold using only data contained in the original image and no assumptions about which experimental parameters influence the threshold, and how. This method is illustrated in Fig. 1 and explained next.

Let S be the original phase-contrast image (Fig. 1a) and $I = |\nabla S|$ its

[1]In phase-contrast microscopy, the magnification influences the imaging artifacts through adjustments of the phase-ring diameter.

gradient, renormalized to intensity values in the interval $[0, 1]$ (Fig. 1b). We then define the threshold function $T : I \times J_u \to K$ as setting all pixels of the image I to 1 if they have intensity values within the interval $J_u = [u, 1]$, and to 0 otherwise. The resulting binary image, thresholded with threshold u, is $T(u) = T(I, J_u)$ (Fig. 1c, inset) and its proportion of non-zero pixels is denoted $P_T(u)$. This proportion monotonically decreases as u increases from 0 to 1 (blue curve in Fig. 1c). For small u, the non-zero pixels will encompass the area around the halo at the edge of the cell plus additional features in the background and inside the cell. As u increases, some pixels around the cell edge drop below u, until the thresholded image $T(u)$ finally does not show a continuous contour of the cell any more (rightmost inset in Fig. 1c). We aim at selecting the largest value of u for which the thresholded image still includes the contiguous contour of the cell. In order to find this value, we compare the thresholded image $T(u)$ with its filled version $T'(u) = T \cup \text{int}(T)$, where $\text{int}(T)$ is the interior of T. The difference between the proportion of non-zero pixels in the filled and thresholded images, $P_{T'}(u) - P_T(u)$ (red curve in Fig. 1c), drops sharply to almost zero when u is large enough to break the contour of the cell edge. At this critical value u^*, the thresholded image $T(u^*)$ contains a non-contractible[2] closed curve entirely lying in non-zero pixels. For thresholds larger than u^* no such curve exists that encloses

[2] not homotopy-equivalent to a point

a non-negligible number of zero-valued pixels. We hence chose u^* as the initial threshold and the filled image $T'(u^*)$ as the initial segmentation mask. The outline of this mask encloses the cell of interest plus a small layer of background pixels around it (see red line in Fig. 2(c1) for an example). It is used as initial contour for the outline refinement algorithm described next.

2.2 Extracting the cell edge using active contours

Starting from this rough segmentation, we find the accurate outline of the cell by evolving a geometric active contour (Kass *et al.*, 1988; Caselles *et al.*, 1993; Malladi *et al.*, 1995; Osher & Sethian, 1988; Chan & Vese, 2001) with a specifically adapted energy functional. The active contour is embedded in a level-set function, defined as the signed-distance function ϕ from the boundary (Sethian, 1999). The cell outline is defined as $\Gamma = \{x|\phi(x) = 0\}$. The level function ϕ is propagated according to the equation of motion $\partial\phi/\partial\tau + v_n|\nabla\phi| = 0$ with a speed function v_n suitably chosen such that the contour Γ converges to the cell outline of interest. In order to determine this speed function, the problem is equivalently formulated as an energy-minimization problem. We evolve ϕ such as to iteratively minimize a certain energy functional that drives Γ toward the cell boundary and penalizes deviations of ϕ from a signed-distance function. Rather than periodically

re-initializing the level set (Sethian, 1999; Chan & Vese, 2002), we choose to embed the signed-distance penalty into the energy functional (Li *et al.*, 2005), thus avoiding implementation of the additional algorithms needed for re-initialization.

The energy to be minimized consists of three components with weights $\lambda > 0$, $\mu > 0$, and ν:

$$\mathcal{E}(\phi) = \mu\mathcal{P}(\phi) + \lambda\mathcal{L}(\phi) + \nu\mathcal{A}(\phi), \text{ with} \tag{1}$$

$$\mathcal{P}(\phi) = \int_S \frac{1}{2}\left(|\nabla\phi| - 1\right)^2 \mathrm{d}\boldsymbol{x} \tag{2}$$

$$\mathcal{L}(\phi) = \int_S g\delta(\phi)\,|\nabla\phi|\,\mathrm{d}\boldsymbol{x} \tag{3}$$

$$\mathcal{A}(\phi) = \int_S gH(-\phi)\mathrm{d}\boldsymbol{x}\,. \tag{4}$$

Here,

$$H(\phi) = \begin{cases} 0 & \text{, if } \phi \leq 0 \\ 1 & \text{, if } \phi > 1 \end{cases}$$

is the *Heaviside distribution* and $\delta(\phi) = H'(\phi)$ the *Dirac delta distribution*, numerically regularized to (Li *et al.*, 2005)

$$\delta_\epsilon(\phi) = \begin{cases} 0 & \text{, if } |\phi| > \epsilon \\ \frac{1}{2\epsilon}(1 + \cos(\frac{\phi\pi}{\epsilon})) & \text{, if } |\phi| \leq \epsilon \end{cases}. \tag{5}$$

The function $g = \frac{1}{1+|\nabla(\boldsymbol{G}_\sigma \star S)|^2}$ is the *edge indicator function*, computed by convolving the original image S with a Gaussian kernel $\boldsymbol{G}_\sigma$ of standard deviation σ.

The total energy combines three contributions: the *internal energy* $\mathcal{P}$, the *line energy* $\mathcal{L}$, and the *area energy* $\mathcal{A}$. The internal energy $\mathcal{P}$ is independent of the image S and only depends on the level-set function ϕ. Its role is to keep ϕ close to a signed distance function during the minimization process. This part of the energy is minimal when $|\nabla\phi| = 1$, i.e., when ϕ is a signed-distance function. The line energy $\mathcal{L}$ drives the contour toward one that has minimum length along a strong edge. More precisely, the contour of minimal length according to the metric $g(\alpha(s))\,|\alpha'(s)|\,\mathrm{d}s$, with $\alpha(s)$ a parametrization of the contour with curvilinear coordinate $s \in [0, 1)$. The area energy $\mathcal{A}$ comprises a surface integral over the interior of the currently estimated outline since the integrand is non-zero only where ϕ is negative. It drives the contour to enclose an edge-free interior, i.e., to minimize the total enclosed amount of the edge indicator function g.

Minimizing the total weighted sum of these three energy components drives the level-set contour Γ to tightly enclose the cell of interest. This is done by iteratively minimizing the total energy $\mathcal{E}$ using gradient descent. Note that if two cells overlap (overcrawl), the gradient descent converges to their joint outline. Denoting by $\frac{\partial\mathcal{E}}{\partial\phi}$ the Gâteaux derivative of the total energy, the following flow locally minimizes $\mathcal{E}$:

$$\frac{\partial\phi}{\partial\tau} = -\frac{\partial\mathcal{E}}{\partial\phi}. \tag{6}$$

The term $\frac{\partial \mathcal{E}}{\partial \phi}$ is found by calculus of variations: for any function $\mathcal{E}(\phi) = \int_S F(\phi, \nabla\phi)\mathrm{d}\boldsymbol{x}$, we necessarily have

$$\frac{\partial F}{\partial \phi} - \sum_i \frac{\partial}{\partial x_i}\left(\frac{\partial F}{\partial \phi_{x_i}}\right) = 0 \tag{7}$$

at extremal points. In order to simplify the notation we write $\phi_{x_i} = \frac{\partial \phi}{\partial x_i}$ for the derivative along the i^{th} direction. Consider a function $F(\phi, |\nabla\phi|)$ that is given by only the internal energy term in Eq. (2). For this choice, the first term in Eq. (7) is zero since F does not explicitly depend on ϕ. The second term evaluates to $-\nabla\cdot\left[(1-\frac{1}{|\nabla\phi|})\nabla\phi\right]$. Applying the same reasoning also for the energy terms in Eqs. (3) and (4), and combining the results, yields:

$$\frac{\partial \mathcal{E}}{\partial \phi} = -\mu\left(\triangle\phi - \nabla\cdot\left(\frac{\nabla\phi}{|\nabla\phi|}\right)\right) - \lambda\left(\delta(\phi)\nabla\cdot\left(g\frac{\nabla\phi}{|\nabla\phi|}\right)\right) - \nu\left(g\delta(\phi)\right)\ . \tag{8}$$

Together with Eq. (6), this defines the iterative process that evolves ϕ such as to perform a gradient-descent minimization of the energy functional $\mathcal{E}$.

The intense and irregular halo surrounding the cells in phase-contrast images causes the edge indicator function to drive the level set to the halo boundary external to the cell (see Fig. 2(c2)). We resolve this by applying a top-hat transform to the original phase-contrast image during an intermediate phase of energy minimization (see Fig. 2(a) for an overview of the procedure). The top-hat transform consist of subtracting the morphological closing of the original image from the original image itself. We use a disk-shaped structuring element with a radius of about the width of the halo.

Figure 2: Figure 2 here

This effectively removes bright features from the images (Serra, 1982) while preserving the original edges. After an initial gradient descent on the unprocessed original image, we switch to the top-hat transformed image, which permits the contour to pass the barrier of the halo without penetrating too deep into the cell (see Fig. 2(c3)). This intermediate stage of the minimization process is then again followed by a gradient descent on the original image, ensuring reliable cell edge detection as shown in Figs. 2(c4) and (d). The numbers of iterations performed on each image are parameters of the algorithm that need to be set by the user. They must be chosen large enough to allow each of the three gradient descents to converge. Choosing them larger than required does not deteriorate the results, but increases the computational time. See Materials and Methods for details about the parameters used here.

2.3 Cell outline tracking

In order to track the dynamic deformations and displacements of the cell outline in a time-lapse sequence of images, the threshold-based segmentation described in Sec. 2.1 only needs to be done for the first image of the sequence (see Fig. 2(a)). For all subsequent frames we construct good candi-

date outlines by using the fact that ϕ is approximately kept a signed-distance function. Evaluating $\phi(x)$ at some positive $x > 0$ we obtain a contour that is further away from the cell edge, but uniformly encloses the cell outline. We choose x large enough to completely enclose the outline of the cell in the next frame. The actual value of x depends on the time-resolution of the movie in relation to the speed of the cell motion. This "inflated" outline is then used as the initial contour for the above-described energy minimization algorithm in the next frame. The overall segmentation and tracking procedure is summarized in Fig. 2(a).

3 Results

The presented algorithm is applied to time-lapse sequences showing polarizing and migrating keratocyte cells. For each frame, the algorithm returns a function ϕ, the zero-level set of which is the contour segmenting the cell from the background. This contour is represented as a set of (x, y) coordinates, resampled such that the contour contains the same number of points in each frame, evenly spaced along the cell outline. The first point (x_0, y_0) is always placed in the same direction from the cell's centroid. The outline is further smoothed by applying a single iteration of the snakedeform.m function (Xu & Prince, 1997) with $\alpha = 2$, $\beta = 10$, $\gamma = 1$, and $\kappa = 0$. This eliminates

small-scale outline undulation resulting from image noise. This representation allows us to characterize each point on the cell contour by its curvilinear coordinate s along the outline, which enables plotting cell-outline properties, such as curvature and edge velocity, as a function of position, time, and distance from the cell centroid.

Before demonstrating the application of the present algorithm to keratocyte phase-contrast movies, we benchmark the accuracy and reliability of the segmentation and tracking procedure on synthetic images with known ground truth.

3.1 Benchmark results

We characterize the efficiency and accuracy of the segmentation procedure on simulated images of different signal-to-noise ratios (SNR) for different cell shapes. We quantify segmentation accuracy by the Dice coefficient, i.e., the proportion of correctly classified pixels with respect to the known ground truth. We then compare the results with the SNR typically obtained in real phase-contrast images in order to assess the consistency of the segmentation and its limitations. The algorithm is implemented in Matlab R2009b using the MEX version of the LSMLIB level-set library (Chu, 2009). Segmenting a 1392×1040 pixels image takes around 500 seconds on a single 2.93 GHz

Intel Core i7 processor.

3.1.1 Generation of artificial images

We generate synthetic benchmark images with precisely known ground truth by simulating the optics of a phase-contrast microscope. We use the physical image-formation model described by Yin *et al.* (2010) with parameters provided by the vendor of the microscope (see Materials and Methods for details). We apply the image-formation model to the black-and-white segmentation masks of different imaged cells, serving as ground-truth objects of different, realistic shapes. We use a total of five different shapes from both polarizing and polarized cells. This procedure leads to the characteristic intensity distribution observed across a cell edge in real phase-contrast images. The resulting image is then corrupted by a combination of multiplicative Poissonian and additive Gaussian noise to mimic the effects of shot noise and read-out noise, respectively. Examples of such simulated synthetic bechmark images are shown in Fig. 3(b) for different SNRs and the cell geometry extracted from Fig. 3(d). The SNR is quantified according to the *Rose criterion*, hence:

$$\mathrm{SNR} = \frac{\mathrm{Prctile}(E)}{\mathrm{Std}(B)}\,, \tag{9}$$

where $\mathrm{Prctile}(E)$ is the 98^{th} percentile of the range of intensities in a region E across the cell edge, and $\mathrm{Std}(B)$ is the standard deviation of intensities in

Figure 3: Figure 3 here

a region B in the image background. In order to more accurately compute these two estimates, they are averaged over five user-selected regions each.

3.1.2 Accuracy of the segmentation

The Dice coefficient in function of the SNR is shown in Fig. 3(a) for five prototypical cell shapes extracted from real images, two examples of which are shown in Figs. 3(c–d). The Rose criterion states that the human eye needs an SNR above 5 in order to be able to distinguish image features with 100% certainly. The Dice coefficient of the present automatic cell outline segmentation rapidly approaches 100% at SNRs between 5 and 6. This indicates that the detection power of the segmentation algorithm is about as good as that of the human eye, making it a viable alternative to manual cell segmentation. The large span between the smallest and largest Dice coefficients observed at SNRs between 5 and 6 is due to random break-down of the threshold-based pre-segmentation at high noise. The SNR of real phase-contrast images is always larger than 10 (see Fig. 3(c–d)), enabling automatic segmentation of cell outlines with more than 99% pixel-level accuracy (Dice coefficient >0.99).

3.2 Application to polarizing and migrating keratocytes

We apply the present segmentation and tracking algorithm to real phase-contrast movies of migrating and polarizing keratocyte cells in order to illustrate the practical applicability of the method and the analyses it enables (see also Supplementary Movie 1). The results allow us to compute quantitative information about the cell dynamics. This includes the cell's centroid position, its migration velocity, the length of the cell outline, the cell's contact surface area, and temporal variations in all of these quantities.

The motion of individual points along the cell contour is used to compute the local edge velocity. Individual points are tracked by assigning to each contour point $c(s,t)$ with curvilinear coordinate s in frame t the point $c(s',t+\Delta t)$ in frame $t+\Delta t$ that minimizes the distance $|c(s',t+\Delta t)-c(s,t)|$. Doing so for each contour point defines the field of displacement $\boldsymbol{d}(s,t) = c(s',t+\Delta t)-c(s,t)$. If the norm of the field of displacement is multiplied with $\mathrm{sign}(\boldsymbol{d}\cdot\boldsymbol{n})$, where $\boldsymbol{n}$ is the outer normal vector onto the cell outline, we obtain protrusion/retraction maps. These maps are a key tool for visualizing qualitative and quantitative information about the cell's movement. Using the curvilinear coordinate s avoids ambiguities caused by strong bending of the cell outline when using angular (cylindrical) coordinates. Strong bending of the outline is frequently observed in polarizing cells (see Fig. 5(a)).

3.2.1 Migrating cells

We apply the present segmentation and analysis methods to a phase-contrast time-lapse movie showing the persistent migration of a polarized cell. Figure 4(a) shows a frame of the movie with the reconstructed cell outlines from the following nine frames overlaid. The trajectory of the cell centroid is shown by the stars.

The corresponding protrusion/retraction map is shown in Fig. 4(c). The black lines highlight the movement of shape features from the side of the retracting rear to its center, as visually confirmed in Fig. 4(b). This illustrates the level of detail that can be achieved in dynamic cell shape analysis using the present segmentation algorithm. The observed behavior is in agreement with the GRE model, which predicts the rearward motion of lateral features during protrusion. A basic assumption of the GRE model is that the shape of the cell does not change as the cell moves forward. This is confirmed by the graphs in Fig. 4(d) and (e), showing that the total length of the outline and the enclosed area vary by less than 5% during migration. Moreover, the mean protrusion profile along the cell edge shows a graded velocity distribution with higher velocities in the center of the leading edge and lower ones on the sides (Fig. 4(f)).

Our analysis thus confirms the predictions of the GRE model for a po-

Figure 4: Figure 4 here

larized cell observed over a sufficiently long time. The fluctuations of the velocity of leading-edge points, however, are around 20% or more of their mean value. This leads us to suggest that the GRE model may not be valid on shorter time scales.

3.2.2 Polarizing cells

The advantages of an accurate automatic segmentation procedure without prior knowledge about the cell shape are most eminently demonstrated when considering polarizing cells. These cells undergo irregular and large deformations, the nature of which is not well understood. No model comparable to the GRE model for migrating cells exists for polarizing cells. This renders protrusion/retraction maps essential for studying cell polarization. Figure 5(a) shows a frame of a phase-contrast time-lapse movie of a polarizing cell with the reconstructed outlines from the following 10 frames overlaid. The same cell after successful polarization is shown in Fig. 5(b). During polarization, the cell's centroid is virtually stationary, but the cell edge undergoes large undulations. The protrusion/retraction map in Fig. 5(c) suggests that these undulations propagate around the cell periphery as waves that are interfering with each other. This is underlined by the red and blue ridges in

Figure 5: Figure 5 here

the protrusion/retraction map traveling around the cell contour at almost constant speed (dashed lines in Fig. 5(c)). The collective interaction of these waves eventually leads to symmetry breaking and polarization of the cell as seen in the protrusion/retraction map around 250 s. During the polarization process both the total edge length and the cell contact surface area increase.

4 Conclusions

We have presented a novel cell outline segmentation algorithm for phase-contrast images that is based on near-optimal thresholding followed by energy-minimizing level-set evolution. The algorithm robustly reconstructs high-resolution outlines from images showing a small number of cells. If two cells overlap (overcrawl), the algorithm fuses them and detects the joint outline. We have suggested a suitable energy functional for phase-contrast images and an iterative algorithm that drives the active contour toward the cell edge. The resulting algorithm allows segmenting the cell outlines in each frame of a time-lapse movie and tracking them over time. This enables the construction of protrusion/retraction maps as a valuable tool for studying cell polarization and migration.

We have benchmarked the efficiency and accuracy of the algorithm on

synthetic images with known ground truth. These images were generated according to a physical image-formation model that describes phase-contrast imaging at various signal-to-noise ratios (Yin *et al.*, 2010). The results have shown that the accuracy of automatic segmentation of phase-contrast images is comparable to that of manual segmentation. At realistic signal-to-noise ratios, as encountered in practical microscopy settings, more than 99% of the image pixels can be expected to be correctly attributed to "cell" or "background".

This allows constructing high-resolution protrusion/retraction maps of both polarizing and migrating cells. These maps are a key tool for observing and visualizing dynamic processes in single-cell biomechanics. When applied to polarized migrating cells, our analysis was able to provide experimental confirmation for the well-established GRE model of cell motility and to confirm established phenomenology at large-enough time scales. When applied to polarizing cells, where no generally accepted model exists, our analysis revealed large-scale protrusion/retraction oscillations along the cell edge that eventually lead to cell polarization. Protrusion/retraction oscillations have previously been observed in other cell types (Machacek & Danuser, 2006; Giannone *et al.*, 2007) and probably represent a more general phenomenon. However, no link to cell polarization has been established before. Automatic characterization of cell-edge behavior during oscillation and polarization in a

large number of phase-contrast image sequences will provide a starting point for a more in-depth analysis and for the formulation of new hypotheses and models.

5 Material and Methods

5.1 Cell culture

Black tetra fish epidermal keratocytes were cultured in Dulbecco's modified Eagle's medium (DMEM; Hepes modification; Sigma Immunochmicals, St. Louis, MO) supplemented with 20% of fetal bovine serum (FBS) and antibiotics as described (Schaub *et al.*, 2007). Briefly the fish scales were extracted with tweezers, placed external side up on dry glass coverslips, and allowed to adhere for 30 to 60 seconds to prevent them from floating. Culture medium was then added and the keratocytes were allowed to migrate to form colonies on the coverslips over night at 30°C. To obtain isolated keratocytes, the cell colonies were treated with 0.2% trypsin and 0.02% EDTA in phosphate-buffered saline (PBS), a solution that breaks cell adhesion to substrate and that was subsequently replaced by fresh culture medium (70%) diluted with distilled water (30%). Cells were then imaged during their transition from the isotropic state to the polarized state. Time-lapse movies of durations

between 1 minute and 1 hour were acquired at 4 frames per second.

5.2 Microscopy

Imaging was done on a Nikon Eclipse TE300 inverted microscope with Nikon 10x, 40x, 60x, and 100x plan objectives. Images were acquired with a CoolSnap HQ2 cooled charge coupled device (CCD) camera (Photometrics, Tucson, AZ) controlled by Metamorph software (Universal imaging, West Chester, PA). Image contrast was enhanced and background features resulting from irregularities of the microscope optics were subtracted as described (Verkhovsky *et al.*, 2003). The optical parameters of the microscope as required by the image-formation model of Yin *et al.* (2010) were provided by Nikon Switzerland, but cannot be disclosed here due to the confidentiality of this information (non-disclosure agreement signed).

5.3 Image analysis

All movies were analyzed using the method presented in this paper. Energy minimization was done using 500 iterations on the original image followed by another 500 iterations on the top-hat transformed image and a final 150 iterations on the original image again. The weights in the energy function in Eq. 1 were set to $\mu = 0.2/\Delta\tau$ and $\lambda = 100$. The parameter ν was set to 0.1

for all iterations on the original image and 10 for all iterations on the top-hat transformed image. Gradient descent on Eq. 6 used a step size of $\Delta\tau = 5$. For stability, it is required that $\mu\,\Delta\tau < 0.25$. The edge indicator function g used $\sigma = 1.5$. The Dirac delta function was regularized using $\epsilon = 1.5$ (see Eq. 5) (Li *et al.*, 2005).

A Matlab implementation of the presented segmentation and tracking algorithm can be downloaded from the web pages of the authors: http://lcb.epfl.ch and http://www.mosaic.ethz.ch.

6 Acknowledgements

We thank many of our colleagues who contributed to this work, in particular M. F. Fournier (LCB, EPF Lausanne), J. Cardinale (MOSAIC Group, ETH Zurich), G. Paul (MOSAIC Group, ETH Zurich), S. Reboux (MOSAIC Group, ETH Zurich), D. Seppey (LCB, EPF Lausanne), C. Bottier (LCB, EPF Lausanne), and B. Vianay (LCB, EPF Lausanne). M.A. was funded by an NCCBI PhD fellowship from the Swiss National Competence Center for Biomedical Imaging, to A.V. and I.F.S. I.F.S. further acknowledges funding from the Swiss SystemsX.ch initiative, grant LipidX-2008/011, evaluated by the Swiss National Science Foundation.

Figure Captions

Figure 1

Illustration of the near-optimal threshold selection procedure. ***(a.)*** Original phase-contrast image of a fish epidermal keratocyte and ***(b.)*** its normalized gradient (contrast adjusted in the figure for visualization purposes only); scale bars are 10 μm. ***(c.)*** Evolution of the coverage of the resulting image in function of the threshold parameter u for the thresholded image $T(u)$ in blue, for its filled version $T'(u)$ in green, and for their difference in red. The images $T(u)$ and $T'(u)$ for three thresholds are shown in the inset panels. The middle panels show the results for the near-optimal threshold u^* as chosen by the algorithm. See main text for details.

Figure 2

Description of the segmentation workflow illustrated with a specific example. ***(a.)*** Workflow of the algorithm; see main text for details. ***(b.)*** Phase-contrast image of a fish epidermal keratocyte; scale bar is 5 μm. ***(c1–4.)*** Magnification of the rectangular region in (b) and (d) with the intermediate contours (red lines) at the end of each of the 4 stages of the algorithm described in (a); scale bars are 5 μm. ***(d.)*** Final cell contour (red line) overlaid on the original phase-contrast image (b).

Figure 3

(a.) Dependence of the Dice coefficient on the image's signal-to-noise ratio (SNR) for different cell shapes. Mean (black curve) and values from individual samples (blue dots) are shown. Red circled dots correspond to the images shown in (b). ***(b.)*** Examples of synthetic benchmark images at different SNRs for the cell shape extracted from subfigure d. ***(c–d.)*** Two examples of the five different cell shapes used as ground truth for the benchmarks. The benchmark set also includes the polarizing cell shape shown in Fig. 5(a). We show the raw phase-contrast images with measured SNRs of 14.2 and 16.6, respectively; scale bars are 5 μm.

Figure 4

Dynamic shape analysis of a polarized keratocyte: 36 frames imaged at a time interval of 4 seconds. ***(a.)*** Phase-contrast image of the cell in frame 13 with the contours (blue lines) extracted from each image up to frame 21. The blue stars represent the cell's centroid computed in each frame. The green/red arrows attached to the contours represent the local protrusion/retraction vectors, respectively. Diamonds and squares mark the positions of the points whose motion is highlighted by the upper and lower black lines in (c), respectively. The scale bar is 5 μm. ***(b1–4.)*** Magnification of the rectangular

region shown in (a) for frames 13, 16, 19, and 21. The black arrows point to two different blobs propagating and evolving along the cell contour. The blob indicated by the vertical arrow corresponds to the diamonds in (a) and the upper black line in (c). ***(c.)*** Protrusion/retraction map as a function of time and contour abscissa (clockwise from the origin $s = 0$ defined as the upper intersection of the contour with the vertical ray emerging from the cell centroid). The map is computed from the norm of the contour displacement; its sign is positive for protrusion and negative for retraction. ***(d.)*** Evolution of the contour length over time. ***(e.)*** Evolution of the cell contact-surface area over time. ***(f.)*** Mean velocity over time (red curve) and its standard deviation (error bars) at the locations of the blue dots shown in (a); the dots are numbered 1 to 30 from top to bottom.

Figure 5

Dynamic shape analysis of a polarizing keratocyte: 80 frames imaged at a time interval of 4 seconds. ***(a.)*** Phase-contrast image of the cell in frame 20 with the contours (blue lines) extracted from each image up to frame 29. The blue stars represent the cell's centroid computed in each frame. The green/red arrows attached to the contours represent the local protrusion/retraction vectors, respectively. The arrow points from the cell centroid

to the origin of the curvilinear coordinate system on the contour (black square on the contour). The scale bar is 10μm. ***(b.)*** The same cell after successful polarization shown for frames 55 to 65. ***(c.)*** Protrusion/retraction map as a function of time and contour abscissa (clockwise from the origin $s = 0$ defined by the intersection of the black arrow in (a) with the contour). The map is computed from the norm of the contour displacement; its sign is positive for protrusion and negative for retraction. Dashed lines indicate protrusion/retraction waves traveling along the cell edge. ***(d.)*** Evolution of the contour length over time. ***(e.)*** Evolution of the cell contact-surface area over time.

Supplementary Movie 1

Example of cell-contour extraction for a polarizing and a polarized keratocyte cell. The movie shows the original phase-contrast videos on the left and the overlay of the video with the extracted contour (red line) on the right. The movie is shown in 20x real time and all videos were acquired as described in the Materials and Methods section. Processing was done using the algorithm and software presented here. Notice that the touching cell in the first part of the video does not distract the contour extraction algorithm.

References

Anderson, K. I. & Cross, R. (2000). Contact dynamics during keratocyte motility. *Curr. Biol.*, **10**, 253–60.

Bradhurst, C., Boles, W. & Xiao, Y. (2009). Segmentation of bone marrow stromal cells in phase contrast microscopy images. In *Image and Vision Computing New Zealand, 2008. IVCNZ 2008. 23rd International Conference*, 1–6. IEEE.

Caselles, V., Catté, F., Coll, T. & Dibos, F. (1993). A geometric model for active contours in image processing. *Numer. Math.*, **66**, 1–31.

Chan, T. & Vese, L. (2001). Active contours without edges. *IEEE Trans. Image Process.*, **10**, 266–77.

Chan, T. & Vese, L. (2002). A level set algorithm for minimizing the Mumford-Shah functional in image processing. In *Variational and Level Set Methods in Computer Vision, 2001. Proc. IEEE Workshop on*, 1, 161–168. IEEE.

Chu, K. T. (2009). LSMLIB. http://ktchu.serendipityresearch.org/software/lsmlib/index.html.

Debeir, O., Adanja, I., Warzee, N., Van Ham, P. & Decaestecker, C. (2008).

Phase contrast image segmentation by weak watershed transform assembly. In *Biomedical Imaging. 5th IEEE Intl. Symp. on*, 724–727. IEEE.

Fournier, M. F., Sauser, R., Ambrosi, D., Meister, J.-J. & Verkhovsky, A. B. (2010). Force transmission in migrating cells. *J. Cell. Biol.*, **188**, 287–97.

Giannone, G., Dubin-Thaler, B., Rossier, O., Cai, Y., Chaga, O., Jiang, G., Beaver, W., Döbereiner, H., Freund, Y., Borisy, G. & Others (2007). Lamellipodial actin mechanically links myosin activity with adhesion-site formation. *Cell*, **128**, 561–575.

Goodrich, H. (1924). Cell behavior in tissue cultures. *Biol. Bull.*, **46**, 252–262.

Grimm, H. P., Verkhovsky, a. B., Mogilner, a. & Meister, J.-J. (2003). Analysis of actin dynamics at the leading edge of crawling cells: implications for the shape of keratocyte lamellipodia. *Eur. Biophys. J.*, **32**, 563–77.

Hand, A., Sun, T., Barber, D. & Hose, D. (2009). Automated tracking of migrating cells in phase-contrast video microscopy sequences using image registration. *J. Microsc.*, **234**, 62–79.

Helmuth, J. A., Burckhardt, C. J., Greber, U. F. & Sbalzarini, I. F. (2009). Shape reconstruction of subcellular structures from live cell fluorescence microscopy images. *J. Struct. Biol.*, **167**, 1–10.

Helmuth, J. A. & Sbalzarini, I. F. (2009). Deconvolving active contours for fluorescence microscopy images. In *Proc. Intl. Symp. Visual Computing (ISVC)*, vol. 5875 of *Lecture Notes in Computer Science*, 544–553. Springer, Las Vegas, USA.

Kass, M., Witkin, A. & Terzopoulos, D. (1988). Snakes: Active contour models. *Int. J. Computer Vision*, 321–331.

Keren, K., Pincus, Z., Allen, G. M., Barnhart, E. L., Marriott, G., Mogilner, A. & Theriot, J. a. (2008). Mechanism of shape determination in motile cells. *Nature*, **453**, 475–80.

Keren, K., Yam, P., Kinkhabwala, A., Mogilner, A. & Theriot, J. (2009). Intracellular fluid flow in rapidly moving cells. *Nat. Cell Biol.*, **11**, 1219–1224.

Lee, J., Ishihara, A., Theriot, J. & Jacobson, K. (1993). Principles of locomotion for simple-shaped cells. *Letters to Nature*, **362**, 168–171.

Li, C., Xu, C., Gui, C. & Fox, M. (2005). Level set evolution without re-initialization: A new variational formulation. *Pattern Recogn.*.

Li, F., Zhou, X., Zhao, H. & Wong, S. (2009). Cell segmentation using front vector flow guided active contours. *Medical Image Computing and Computer-Assisted Intervention–MICCAI*, 609–616.

Li, K., Miller, E., Chen, M., Kanade, T., Weiss, L. & Campbell, P. (2008). Cell population tracking and lineage construction with spatiotemporal context. *Med. Image Anal.*, **12**, 546–566.

Machacek, M. & Danuser, G. (2006). Morphodynamic profiling of protrusion phenotypes. *Biophys. J.*, **90**, 1439–52.

Malladi, R., Sethian, J. & Vemuri, B. (1995). Shape modeling with front propagation: A level set approach. *Pattern Analysis and Machine Intelligence, IEEE Trans. on*, **17**, 158–175.

Mitchison, T. (1996). Actin-based cell motility and cell locomotion. *Cell*, **84**, 371–379.

Mogilner, A. & Oster, G. (1996). Cell motility driven by actin polymerization. *Biophys. J.*, **71**, 3030–3045.

Mogilner, A. & Oster, G. (2003). Polymer motors: pushing out the front and pulling up the back. *Curr. Biol.*, **13**, R721–R733.

Osher, S. & Sethian, J. (1988). Fronts propagating with curvature-dependent speed: algorithms based on Hamilton-Jacobi formulations. *J. Comput. Phys.*, **79**, 12–49.

Otaki, T. (2000). Artifact Halo Reduction in Phase Contrast Microscopy Using Apodization. *Opt. Rev.*, **7**, 119–122.

Pantaloni, D., Clainche, C. & Carlier, M. (2001). Mechanism of actin-based motility. *Science*, **292**, 1502–1506.

Pincus, Z. & Theriot, J. a. (2007). Comparison of quantitative methods for cell-shape analysis. *J. Microsc.*, **227**, 140–56.

Russell, R. a., Adams, N. M., Stephens, D. a., Batty, E., Jensen, K. & Freemont, P. S. (2009). Segmentation of fluorescence microscopy images for quantitative analysis of cell nuclear architecture. *Biophys. J.*, **96**, 3379–89.

Satulovsky, J., Lui, R. & Wang, Y.-l. (2008). Exploring the control circuit of cell migration by mathematical modeling. *Biophys. J.*, **94**, 3671–83.

Schaub, S., Bohnet, S., Laurent, V., Meister, J. & Verkhovsky, A. (2007). Comparative maps of motion and assembly of filamentous actin and myosin II in migrating cells. *Mol. Biol. Celll*, **18**, 3723.

Serra, J. (1982). *Image Analysis and Mathematical Morphology*, vol. 1. Academic Press.

Sethian, J. A. (1999). *Level Set Methods and Fast Marching Methods*. Cambridge University Press, Cambridge, UK.

Svitkina, T., Verkhovsky, A., McQuade, K. & Borisy, G. (1997). Analysis

of the actin-myosin II system in fish epidermal keratocytes: mechanism of cell body translocation. *J. Cell Biol.*, **139**, 397.

Verkhovsky, A., Svitkina, T. & Borisy, G. (1999). Network contraction model for cell translocation and retrograde flow. *Biochem. Soc. Symp.*, **65**, 207–22.

Verkhovsky, A. B., Chaga, O. Y., Schaub, S., Svitkina, T. M., Meister, J.-J. & Borisy, G. G. (2003). Orientational order of the lamellipodial actin network as demonstrated in living motile cells. *Mol. Biol. Cell*, **14**, 4667–75.

Xu, C. & Prince, J. (1997). Gradient vector flow: a new external force for snakes. *Proc. IEEE Conf. Computer Vision and Pattern Recognition (CVPR)*, 66–71.

Yam, P. T., Wilson, C. a., Ji, L., Hebert, B., Barnhart, E. L., Dye, N. a., Wiseman, P. W., Danuser, G. & Theriot, J. a. (2007). Actin-myosin network reorganization breaks symmetry at the cell rear to spontaneously initiate polarized cell motility. *J. Cell Biol.*, **178**, 1207–21.

Yin, Z., Li, K., Kanade, T. & Chen, M. (2010). Understanding the optics to aid microscopy image segmentation. *Medical Image Computing and Computer-Assisted Intervention–MICCAI*, 209–217.

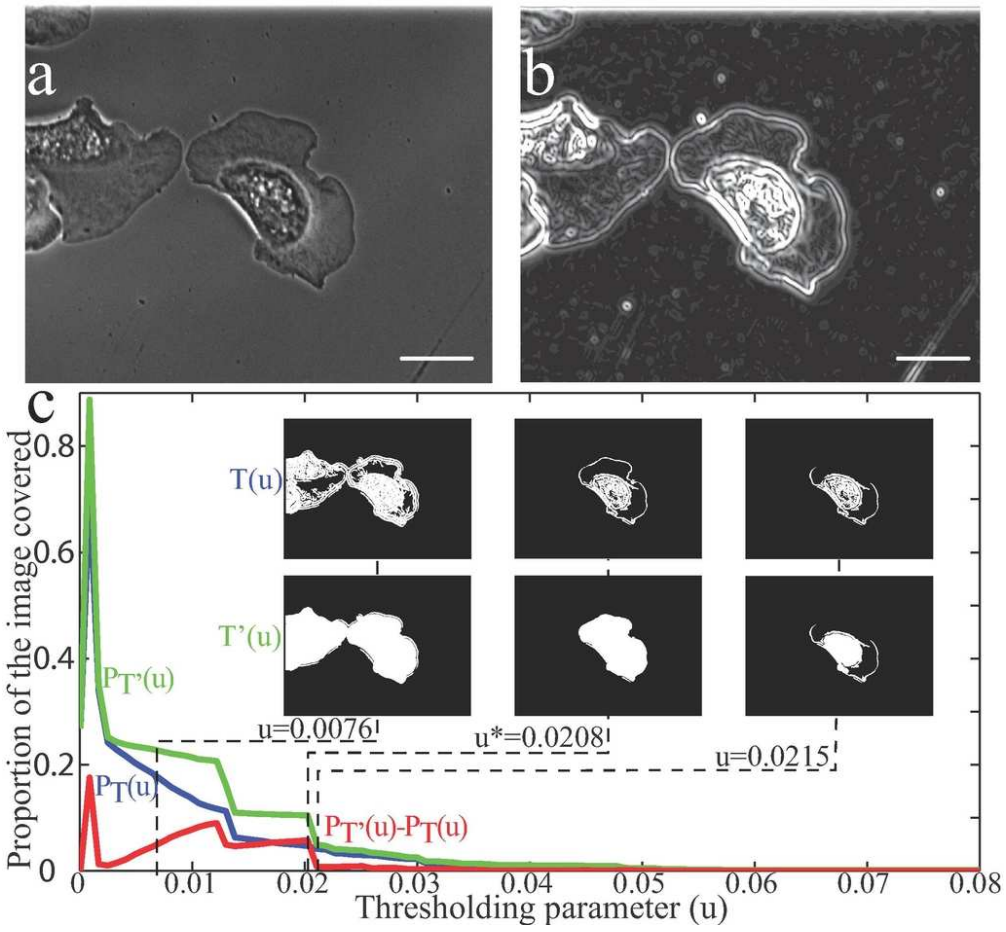

87x81mm (300 x 300 DPI)

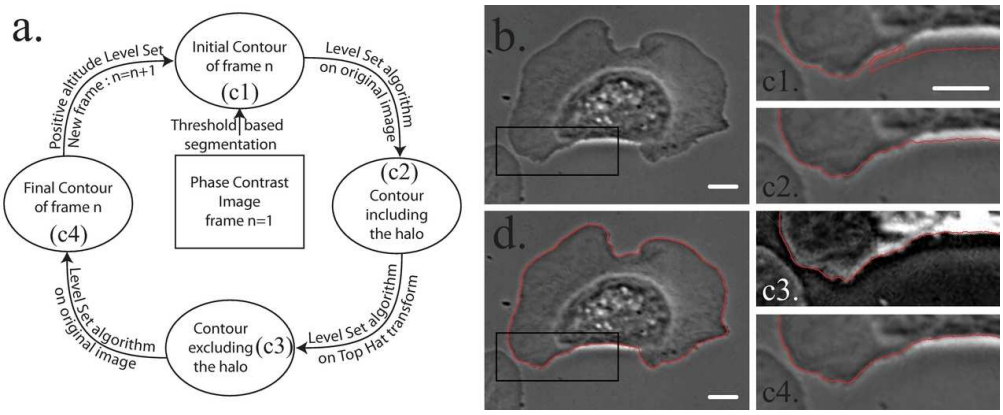

107x43mm (300 x 300 DPI)

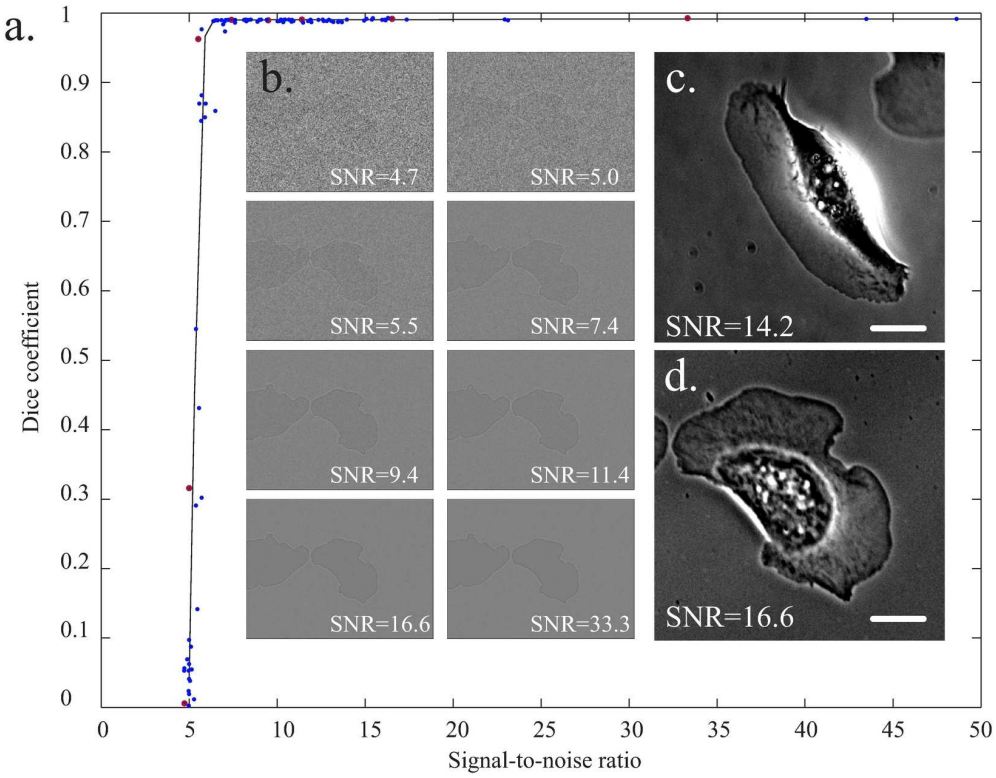

139x108mm (300 x 300 DPI)

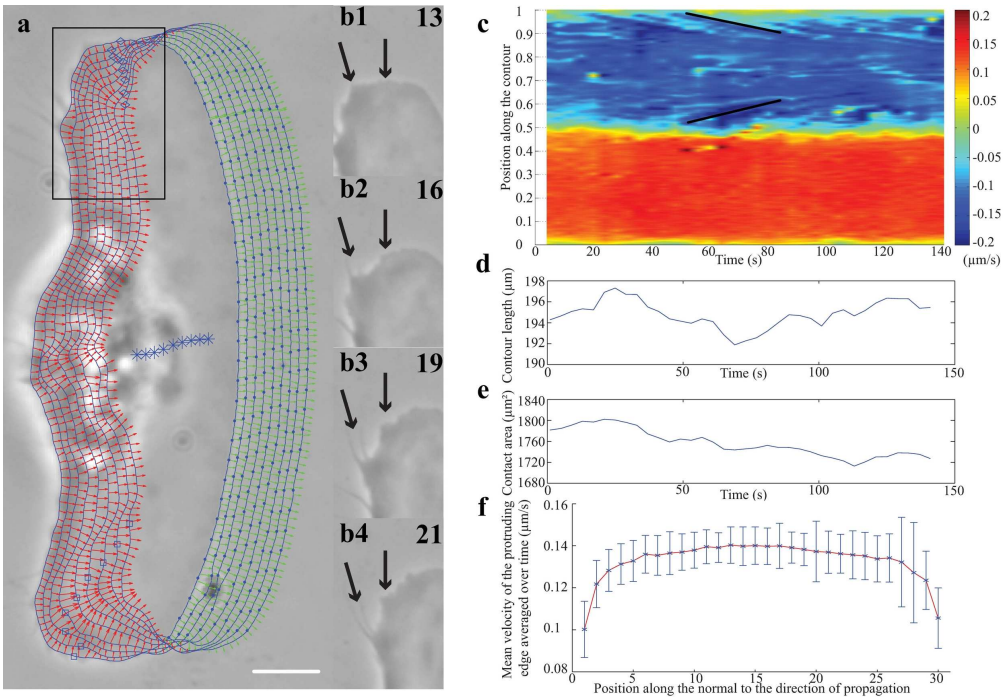

210x145mm (300 x 300 DPI)

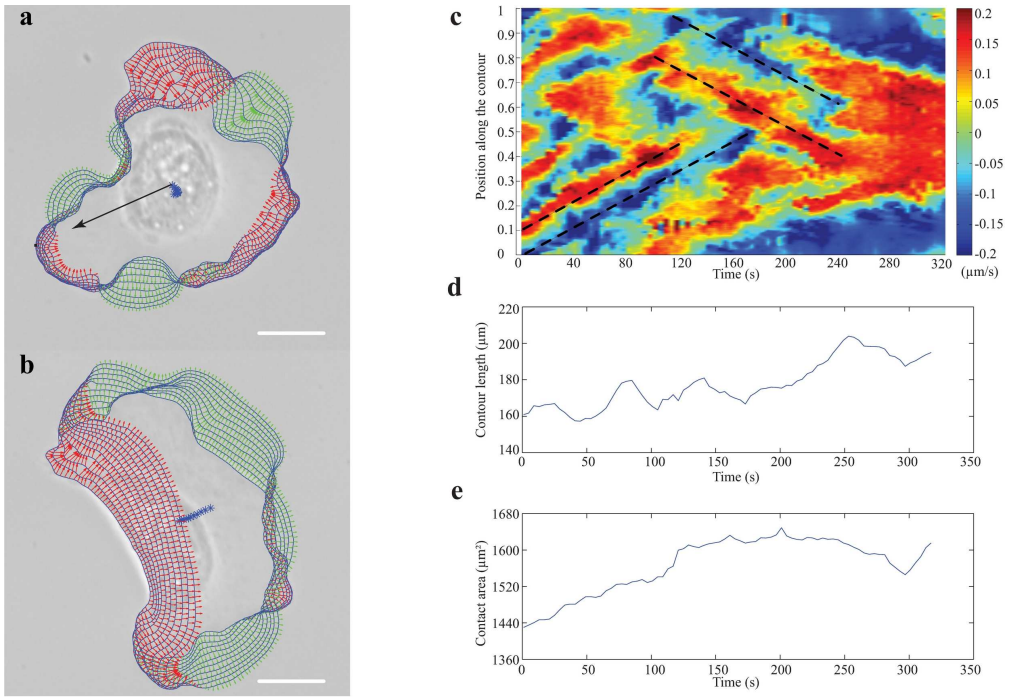

209x145mm (300 x 300 DPI)